toxics

MDPI

Article

Persulfate–Based Advanced Oxidation Process for Chlorpyrifos Degradation: Mechanism, Kinetics, and Toxicity Assessment

Youxin Xu [1,2], Chenxi Zhang [2], Haobing Zou [2], Guangrong Chen [2], Xiaomin Sun [3], Shuguang Wang [1,4,*] and Huifang Tian [1,*]

[1] Institute of Environmental Biotechnology and Functional Materials, School of Environmental Science and Engineering, Shandong University, Qingdao 266237, China; xuyouxin@wfust.edu.cn
[2] Shandong Engineering Laboratory for Clean Utilization of Chemical Resources, Weifang University of Science and Technology, Weifang 262700, China; sdzhangcx@gmail.com (C.Z.); A15910058268@outlook.com (H.Z.); guangrongchen2004@outlook.com (G.C.)
[3] Environment Research Institute, Shandong University, Qingdao 266237, China; sxmwch@sdu.edu.cn
[4] Sino-French Research Institute for Ecology and Environment (ISFREE), Shandong University, Qingdao 266237, China
* Correspondence: wsg@sdu.edu.cn (S.W.); hftian@sdu.edu.cn (H.T.)

Abstract: Persulfate-based advanced oxidation process has been proven to be a promising method for the toxic pesticide chlorpyrifos (CPY) degradation in wastewater treatment. However, due to the limitation for the short-lived intermediates detection, a comprehensive understanding for the degradation pathway remains unclear. To address this issue, density functional theory was used to analyze the degradation mechanism of CPY at the M06-2X/6-311++G(3df,3pd)//M06-2X/6-31+G(d,p) level, and computational toxicology methods were employed to explore the toxicity of CPY and its degradation products. Results show that hydroxyl radicals (·OH) and sulfate radicals ($SO_4^{\bullet-}$) initiate the degradation reactions by adding to the P=S bond and abstracting the H atom on the ethyl group, rather than undergoing α-elimination of the pyridine ring in the persulfate oxidation process. Moreover, the addition products were attracted and degraded by breaking the P–O bond, while the abstraction products were degraded through dealkylation reactions. The transformation products, including 3,5,6-trichloro-2-pyridynol, O,O-diethyl phosphorothioate, chlorpyrifos oxon, and acetaldehyde, obtained through theoretical calculations have been detected in previous experimental studies. The reaction rate constants of CPY with ·OH and $SO_4^{\bullet-}$ were 6.32×10^8 and 9.14×10^8 $M^{-1} \cdot s^{-1}$ at room temperature, respectively, which was consistent with the experimental values of 4.42×10^9 and 4.5×10^9 M^{-1} s^{-1}. Toxicity evaluation results indicated that the acute and chronic toxicity to aquatic organisms gradually decreased during the degradation process. However, some products still possess toxic or highly toxic levels, which may pose risks to human health. These research findings contribute to understanding the transformation behavior and risk assessment of CPY in practical wastewater treatment.

Keywords: chlorpyrifos; persulfate-based advanced oxidation process; degradation mechanisms; theoretical prediction; ecotoxicity assessment

Citation: Xu, Y.; Zhang, C.; Zou, H.; Chen, G.; Sun, X.; Wang, S.; Tian, H. Persulfate–Based Advanced Oxidation Process for Chlorpyrifos Degradation: Mechanism, Kinetics, and Toxicity Assessment. *Toxics* **2024**, *12*, 207. https://doi.org/10.3390/toxics12030207

Academic Editors: Xueqing Shi, Weilong Song, Binghan Xie and Roberto Rosal

Received: 20 February 2024
Revised: 5 March 2024
Accepted: 7 March 2024
Published: 9 March 2024

1. Introduction

Chlorpyrifos (CPY) is a type of organophosphorus pesticides with broad-spectrum biological activity, which is widely used in various agricultural and horticultural crops as well as in households to combat biting and stinging pests [1–3]. In 2018, the annual production of CPY reached 28,600 tonnes, and the global demand for this insecticide has an increasing trend year by year [4]. According to the classification of the World Health Organization, CPY belongs to the second category of pesticides with moderate toxicity [5]. The half-life of CPY ranges from 10 to 120 days, depending on the surrounding environment [6]. Decades of monitoring researchers have reported that CPY levels in seawater, rivers, groundwater,

and even rainwater in different countries exceed permissible levels [7,8]. The concentration of CPY can reach to 303.8 $\mu g \cdot L^{-1}$, far exceeding the environmental allowable limits in the United States and Canada [4]. Researchers have found that CPY can cause liver and gill tissue damage in carp with low concentrations in aquatic environments [9]. Furthermore, once exposed in CPY, humans and animals can also cause reproductive and developmental neurotoxicity risks [10–13]. Because of the persistence and potential ecological hazards of CPY in water environments, methods for its removal have been attracted considerable attention.

Different techniques such as adsorption, microbial degradation, and nanophotocatalysis have been proven effective in removing CPY from water environments [14–16]. However, these methods have certain limitations. Adsorption materials may pose environmental risks [17,18], microbial degradation processes are relatively slow [19,20], and nanophotocatalysis materials also face issues with recovery and reusability [21,22]. In recent years, persulfate-based advanced oxidation processes (AOPs) have gained increasing attention. This is because sulfate radicals ($SO_4^{\bullet-}$) generated by persulfate have longer half-lives, higher redox potentials, and better selectivity compared to hydroxyl radicals (·OH) [23,24]. Shah et al. prepared Fe-ZnO using the sol-gel method and used it in activating the persulfate process; results demonstrated that the generation of high concentrations of $SO_4^{\bullet-}$ and ·OH have strong oxidation effect on CPY degradation [25]. Xie et al. found that CPY presents a rapid removal rate and almost completely degraded with the ultrasound-activated persulfate process [26]. This study proposed that the removal mechanism of CPY could be divided into two possible degradation pathways. The first possible pathway is the α-dechlorination of pyridine molecular fragments under the attack of ·OH; the second possible degradation pathway is the breaking of the bond between phosphorus and oxygen connected to the pyridine ring by ·OH, resulting in the formation of chloropyridine and diethylthiophosphoric acid. Shang et al. explored the degradation effect of the combination of microwave and persulfate on CPY in soil and explored the oxidation of $SO_4^{\bullet-}$ and ·OH, speculating on the process of oxidation, dealkylation, and dealkylation-hydroxylation [27]. However, due to the limitations in detection instruments, the existence of some short-lived intermediates during the degradation process may be not be detected. Therefore, the specific degradation pathways are still unclear and require further research and discussion.

Density functional theory (DFT) has been widely applied to study the chemical reaction mechanisms through elementary reactions [28,29]. DFT calculations can verify the existence of short-lived intermediates during the reaction process. Zhou et al. investigated the reaction mechanism and potential degradation products of CPY induced by ·OH in the atmosphere at the level of MPWB1K/6-311+G(3df,2p) //MPWB1K/6-31G(d) [30]. Theoretical studies indicate that ·OH addition to P atom, dehydrogenation of the -CH_2- portion, and hydroxylation at the C atom in the pyridine ring are energetically favorable pathways for the reaction of CPY with ·OH. The main products of atmospheric oxidation are chlorpyrifos oxide, SO_2, 3,5,6-tetrachloro-2-pyridinol, and O,O-diethyl phosphorothioate. Zhao et al. studied the degradation reaction mechanisms of two representative organophosphorus pesticides, namely mevinphos and monocrotophos, in the presence of ·OH in the atmosphere and water using quantum chemical methods [31].

The study aimed to establish the reaction rate constants, the degradation mechanism, and degradation products of CPY with $SO_4^{\bullet-}$ and ·OH from persulfate using quantum chemical methods. With the degradation of CPY and the generation of the degradation products, it is anticipated that the eco-toxicity may made changes. Computational toxicology method is a valuable technique for the rapid screening of toxic substances, which can be used for the toxicity prediction of transformation products of organic pollutants in water environments [32,33]. In this study, the computational toxicology method is employed to predict the eco-toxicity of CPY and its products in water environments, aiming to estimate their potential environmental risks. The obtained theoretical results will help us better understand the degradation of CPY in sulfate-based AOPs and cover the shortage of experimental data in the CPY degradation processes.

2. Computational Methods

2.1. Mechanism Calculations

In this study, the quantum chemical calculations for all the geometry optimizations involved in the degradation process were performed using the Gaussian 16 program [34]. The geometric configurations of all the reactants, intermediates (IM), transition states (TS), and products (P) were optimized at the M06-2X/6-31+G(d,p) level. M06-2X has been proven to be a reliable method for calculating the transformation mechanisms and kinetics of organic pollutants [35]. Additionally, frequency analysis was performed on the optimized structures with the same method and basis set level to ensure that the structures corresponded to local minima and transition states with only one imaginary frequency. The rationality of the transition state structures was thoroughly confirmed by intrinsic reaction coordinate (IRC) analysis, which connected each transition state with its corresponding reactants and products [36]. Furthermore, to obtain more accurate energies, single-point energy calculations were carried out at the M06-2X/6-311++G(3df,3pd) level for all the structures. In order to account for the solvent effect in the entire system, the SMD model was employed [37]. This model is a novel continuum solvent model based on the self-consistent reaction field (SCRF) theory, where "d" stands for "density" and represents the utilization of the entire solute electron density without defining partial atomic charges. It is considered a more accurate method and has been successfully applied in some aqueous reactions involving $SO_4^{\bullet-}$ and ·OH [38,39].

2.2. Kinetics Calculations

The kinetics results could be obtained from the KisThelP program, which is based on the Transition State Theory (TST) with Wigner tunneling correction [40,41]. Equation (1) shows the thermodynamic equivalent (k^{TST}) using KiSThelP [40]:

$$k^{TST}(T) = \sigma \frac{k_b T}{h} \left(\frac{RT}{p^0}\right)^{\Delta n} e^{-\frac{\Delta G^{0,\neq}(T)}{k_b T}} \quad (1)$$

where σ is the reaction path degeneracy, k_b is the Boltzmann's constant, T is the temperature, h is the Planck's constant, and $\Delta G^{0,\neq}(T)$ represents the standard Gibbs free energy of activation for the considered reaction.

When the reaction involved precursor complex (PRC), the reaction rate constants were calculated using the following formula [42]:

$$R_1 + R_2 \underset{K_{eq}}{\longleftrightarrow} PRC \underset{k_1}{\longrightarrow} P \quad (2)$$

$$k = K_{eq} \times k_1 \quad (3)$$

where K_{eq} represents the equilibrium constant for fast pre-equilibrium between the reactants and k_1 represent the unimolecular reaction. The thermodynamic expression of the K_{eq} is employed in KiSThelP, as described in Equation (4) as follows [40]:

$$K_{eq} = e^{-\frac{\Delta G^0(T)}{RT}} \quad (4)$$

In the formula, $\Delta G^0(T)$ is the associated standard reaction Gibbs energy at temperature T and R is the ideal gas constant.

2.3. Eco-Toxicity Assessment

The toxicity assessment of CPY and its degradation products were determined using the quantitative structure-activity relationship (QSAR) based Ecological Structure Activity Relationship (ECOSAR V2.2) predictive model [43]. Fish, dephnia, and green algae were selected as aquatic organisms to evaluate acute and chronic toxicity risks. The acute toxicity for fish and daphnia was determined using the median lethal concentration (LC50), which

means 50% lethal concentration of fish and daphnia after 96 and 48 h exposure, respectively. The acute toxicity for green algae was determined with the median effect concentration (EC50), which means 50% effective concentration of green algae after 96 h exposure. The chronic toxicity value (ChV) was used to reflect the chronic toxicity for three aquatic organisms. In addition, the toxicity evaluation software tool (TEST V5.1.1) was used to assess the bioaccumulation factor, developmental toxicity mutagenicity of CPY, and its degradation products [44].

3. Results and Discussion

To validate the computational model, the bond lengths of the CPY molecule at the M06-2X/6-31+G(d,p) level were calculated (Table S1). The calculated results are in good agreement with experimental values, with deviations of the calculated bond lengths from the experimental values within 5% [45]. These results demonstrate the reliability of the computational level and the CPY model.

3.1. CPY Structure Analysis

In order to have a clear and description, all atoms have been labeled, and the structure of CPY is shown in Figure 1a. It can be seen that CPY contains a pyridine ring, a P=S bond, and two ethyl groups. To predict the reaction site, the average localized ionization energy of CPY was calculated, and the results of Fukui function and dual descriptor were analyzed, as shown in Figure 1b,c.

(a)

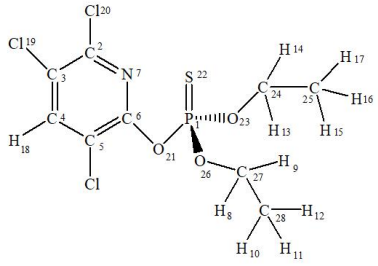

(b)

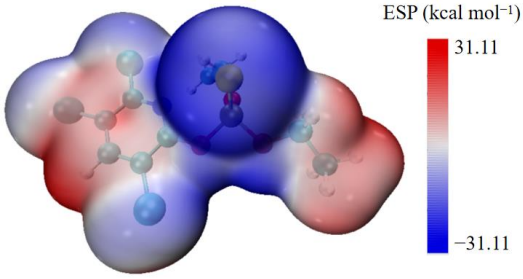

(c) Condensed f^0 and CDD indices for CPY

Atom	f^0	CDD	Atom	f^0	CDD
1(P)	0.0185	−0.0330	16(H)	0.0121	−0.0025
2(C)	0.0543	0.0344	17(H)	−0.0035	−0.0062
3(C)	0.0422	−0.0123	18(H)	0.0457	0.0480
4(C)	0.0795	0.1164	19(Cl)	0.0967	−0.0150
5(C)	0.0549	0.0241	20(Cl)	0.0973	0.0197
6(C)	0.0392	0.0255	21(Cl)	0.1053	0.0111
7(N)	0.0562	0.0950	22(O)	0.0354	−0.0373
8(H)	0.0061	0.0016	23(S)	0.1576	−0.2190
9(H)	0.0066	−0.0022	24(O)	0.0149	-0.0203
10(H)	0.0047	−0.0027	25(C)	0.0037	-0.0018
11(H)	0.0124	−0.0034	26(C)	0.0059	−0.0027
12(H)	0.0061	−0.0042	27(O)	0.0080	−0.0111
13(H)	0.0153	0.0017	28(C)	0.0049	−0.0000
14(H)	−0.0012	−0.0023	29(C)	0.0059	−0.0030
15(H)	0.0145	0.0000			

Figure 1. (**a**) The structure of Chlorpyrifos. (**b**) Molecular surface electrostatic potential distribution diagram of CPY. (**c**) Condensed f^0 andCDD indices for CPY.

Figure 1b shows that the bluer the color, the more negative the electrostatic potential; and the redder the area, the more positive the electrostatic potential. Additionally, when the molecular surface electrostatic potential value became smaller, the electron reactivity became stronger, resulting in electrophilic and radical reactions. Figure 1b also shows that the electrostatic potential map of CPY confirmed that the P=S bond region is a relatively electron-deficient active region, which is easily attacked by active radicals. The pyridine ring and ethyl regions of CPY tend to be attacked by nucleophiles.

Figure 1c shows the Fukui function (f^0) and dual descriptor analysis (CDD). The region with the highest f^0 is the easiest one to be attacked by active radicals, and for the CDD, the region with the largest negative value is the easiest to be attacked by electrophiles [46]. The

most prominent area of f^0 is located at S_{22}, indicating that these sites should be easy to be attacked by active radicals. In addition, according to the CDD, S_{22} is the most negative site, which means that the site should be the easiest to be attacked by electrophiles. Therefore, both methods indicate that the P=S bond in CPY is the most vulnerable to be attacked by ·OH and $SO_4^{\bullet-}$.

Furthermore, ·OH and $SO_4^{\bullet-}$ have strong oxidizing properties, and they can easily undergo addition reactions with unsaturated bonds and abstraction reactions with H atoms [28,29]. Therefore, it is considered that the addition reactions of radicals with the P=S bond and pyridine ring, as well as the abstraction reactions with H atoms.

3.2. The Reaction of CPY with the ·OH

Figures 2 and 3 show the addition and abstraction reactions of CPY with ·OH, respectively. The optimized chemical conformations of TS for CPY with ·OH are shown in Figure S1. Here, $\Delta G^{\neq}$ represents the Gibbs free energy barrier, and ΔrG represents the Gibbs free energy change of the reaction.

The addition reaction of the ·OH with the P=S bond in CPY first forms PRC1, releasing 6.62 kcal mol^{-1} of heat. The configuration of PRC1 is shown in Figure S1. Then, it proceeded through transition state TS1-1(OH), which had a very low Gibbs free energy barrier of only 1.96 kcal mol^{-1}. The ΔrG is −14.34 kcal·mol^{-1}, indicating that the reaction could occur spontaneously.

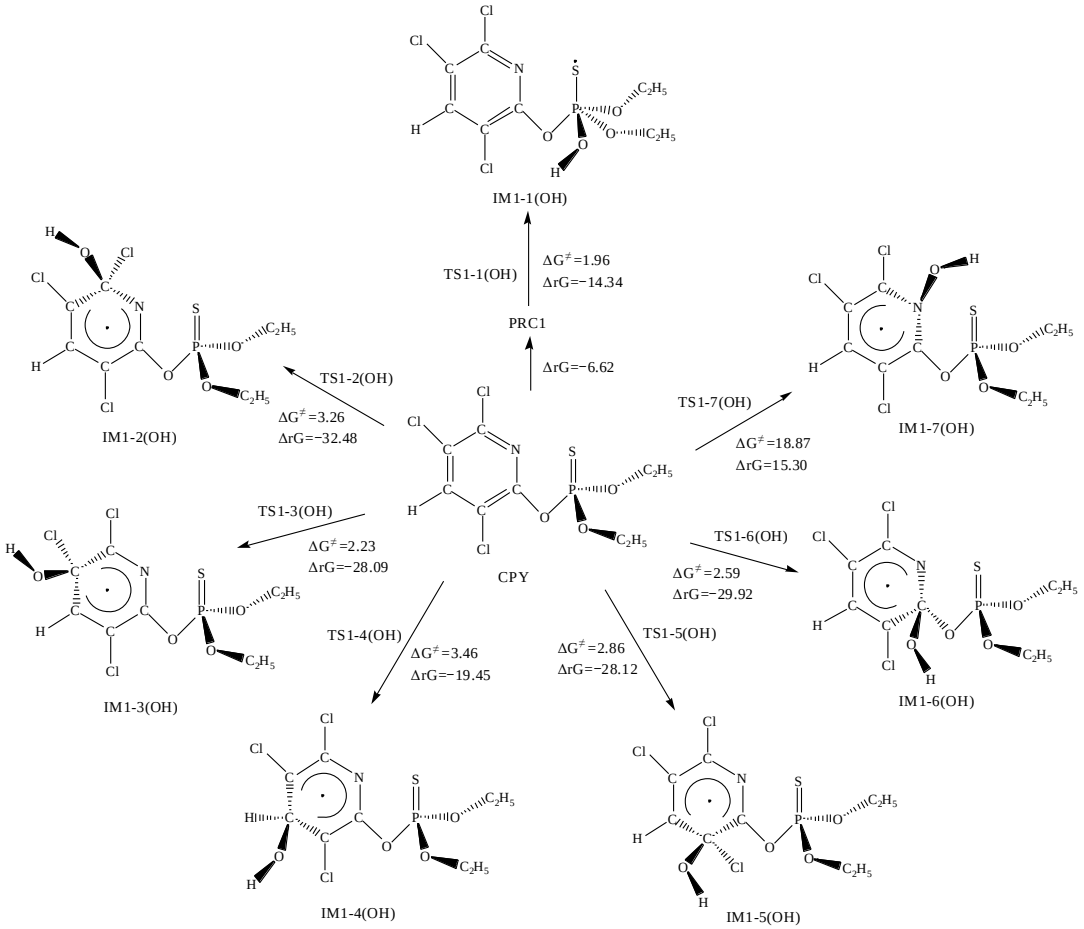

Figure 2. The Gibbs free energy barrier $\Delta G^{\neq}$ (kcal·mol^{-1}) and the Gibbs free energy change ΔrG (kcal·mol^{-1}) at 298 K for ·OH addition pathways with CPY.

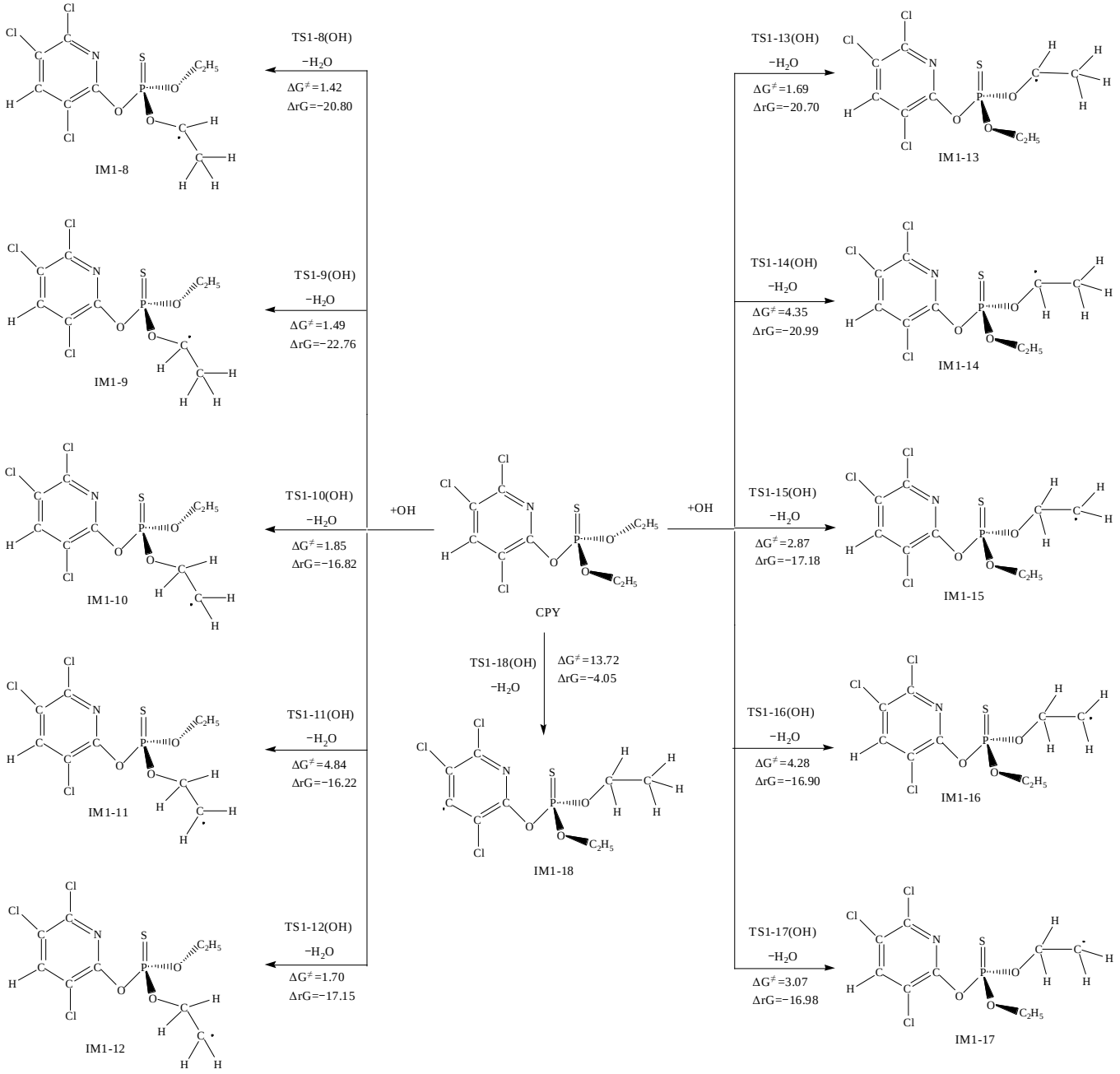

Figure 3. The Gibbs free energy barrier $\Delta G^{\neq}$ (kcal·mol^{-1}) and the Gibbs free energy change ΔrG (kcal·mol^{-1}) at 298 K for ·OH abstraction pathways with CPY.

Since the pyridine ring has six delocalized π electrons, the ·OH could attach to atoms C_2, C_3, C_4, C_5, C_6, and N_7. By comparing the Gibbs free energy barriers, it is found that the addition to the C atoms had relatively low barriers ranging from 2.23 to 3.46 kcal·mol^{-1}, and the free energy changes were negative, leading to spontaneous reactions. However, the addition to the N_7 atom had a higher $\Delta G^{\neq}$ of 18.87 kcal·mol^{-1} and a positive ΔrG of 15.30 kcal·mol^{-1}, indicating that it could not occur spontaneously at room temperature.

In addition, the ·OH could also abstract H atoms from CPY, including the H atoms on the two ethyl groups and the H atom on the pyridine ring. All the abstraction reactions have been calculated (Figure 3). By comparing the $\Delta G^{\neq}$ and ΔrG, it be observed that the barriers for the H atoms on the ethyl groups are relatively low, ranging from 1.42 to 4.84 kcal·mol^{-1}, while the barrier for the pyridine ring was relatively high at 13.72 kcal·mol^{-1}. All the

energy changes were negative, indicating that spontaneous reactions could be occurred at room temperature.

Overall, from a thermodynamic perspective, except for the reaction with N_7 atoms having a high $\Delta G^{\neq}$ and being non-spontaneous, the other addition and abstraction reactions could occur spontaneously.

3.3. The Reaction between CPY and the $SO_4^{\bullet-}$

The mechanism of the reaction initiated by $SO_4^{\bullet-}$ was similar to that of CPY with ·OH, including addition reactions and H abstraction reactions. The $\Delta G^{\neq}$ and ΔrG for $SO_4^{\bullet-}$ addition pathways and abstraction pathways with CPY are shown in Figures 4 and 5, respectively. The optimized chemical conformations of TS for CPY with $SO_4^{\bullet-}$ are shown in Figure S2.

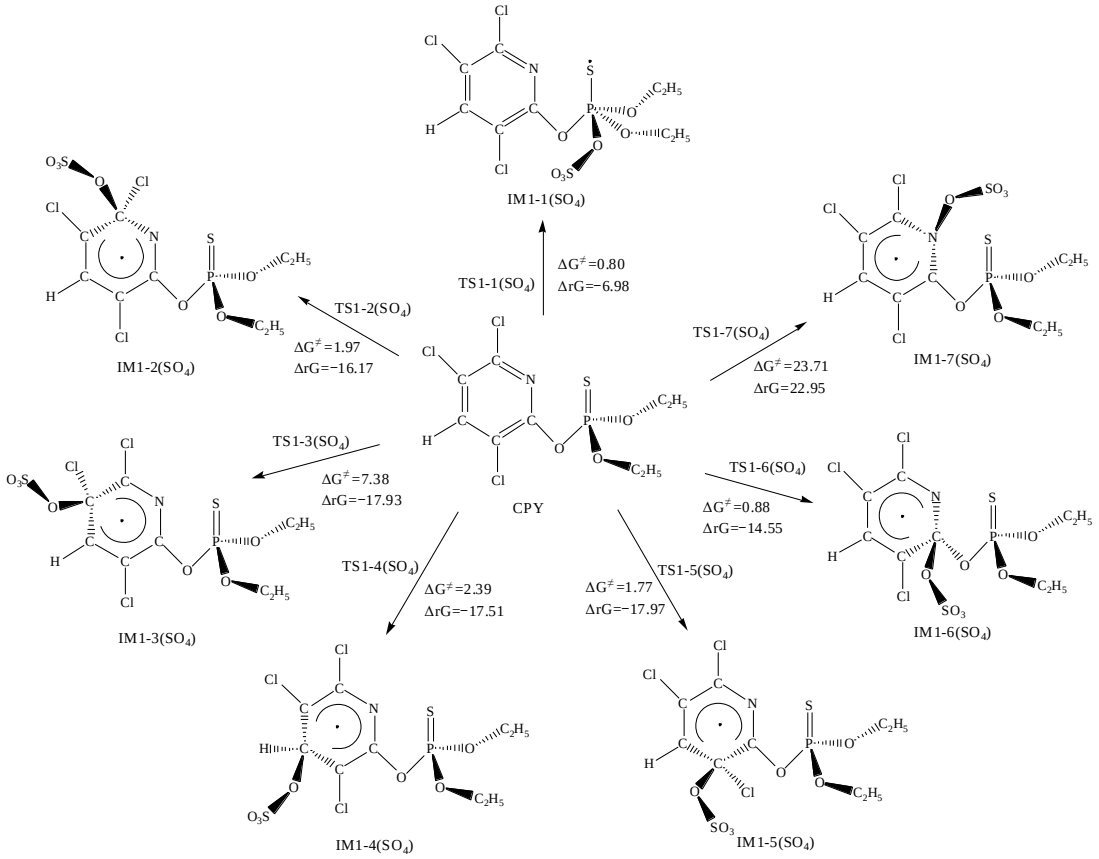

Figure 4. The Gibbs free energy barrier $\Delta G^{\neq}$ (kcal·mol^{-1}) and the Gibbs free energy change ΔrG (kcal·mol^{-1}) at 298 K for $SO_4^{\bullet-}$ addition pathways with CPY.

For the addition reaction of $SO_4^{\bullet-}$, the most likely site is the P=S bond, with a $\Delta G^{\neq}$ of 0.80 kcal·mol^{-1}, and releasing 6.98 kcal·mol^{-1} of energy. Additionally, the addition reactions to the C atoms in the pyridine ring had low barriers ranging from 0.88 to 7.38 kcal·mol^{-1}. However, the addition reaction to the N_7 atom had a high $\Delta G^{\neq}$ of 23.71 kcal·mol^{-1} and a positive ΔrG, indicating that it could not occur spontaneously at room temperature.

Furthermore, as shown in Figure 5, $SO_4^{\bullet-}$ can abstract H atoms connected to the C atoms, forming $HSO_4^{\bullet-}$. By comparing the $\Delta G^{\neq}$ for the H abstraction reactions at different positions, the H atom connected to the C atom bonded with O was most easily abstracted, with barriers ranging from 3.32 to 4.51 kcal·mol^{-1}. Next is the abstraction from the methyl group, with a barrier between 6.97 to 10.52 kcal·mol^{-1}. Moreover, the H atom on the

pyridine ring was the most difficult to abstract, with a $\Delta G^{\neq}$ of 20.59 kcal·mol^{-1} and a positive ΔrG, indicating it could not occur spontaneously at room temperature.

Overall, from the view of thermodynamics, except for the addition reaction to N_7, the abstraction of H atoms on the pyridine ring had high $\Delta G^{\neq}$, which was not easy to occur spontaneously at room temperature, the other addition and abstraction reactions could occur spontaneously. For a further exploration and evaluation for the likelihood of the reactions and the contribution of each reaction pathway, kinetic calculations for each elementary reaction comparing the magnitudes of the rate constants to determine the optimal pathway were performed.

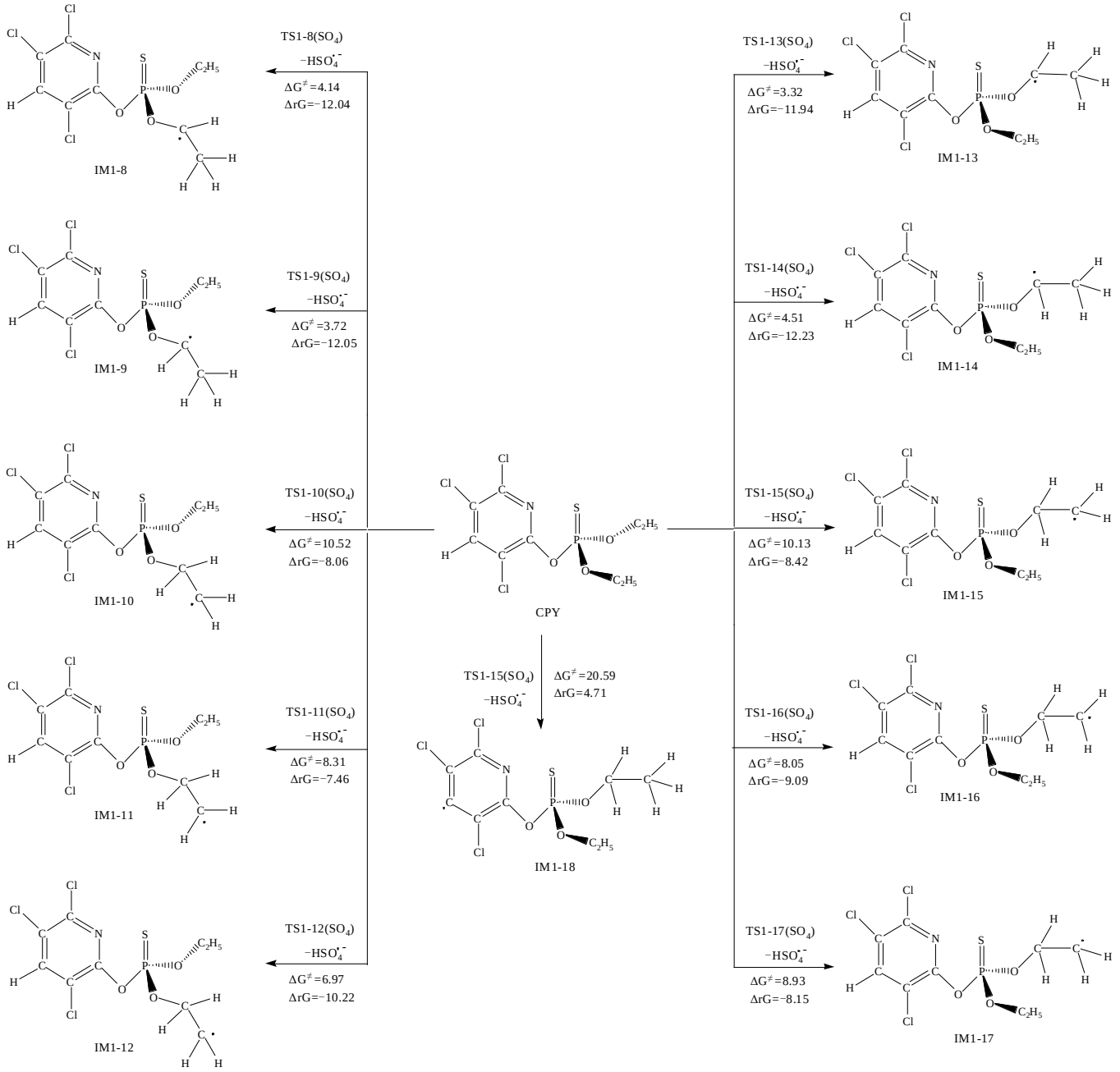

Figure 5. The Gibbs free energy barrier $\Delta G^{\neq}$ (kcal·mol^{-1}) and the Gibbs free energy change ΔrG (kcal·mol^{-1}) at 298 K for $SO_4^{\bullet-}$ abstraction pathways with CPY.

3.4. Rate Constants Calculation

The rate constants (k) for the initiation reactions of CPY by ·OH and $SO_4^{\bullet-}$ were calculated at 298 K, including all possible addition and abstraction reactions. The calculated results are shown in Table 1, where k_{add} represents the rate constants for addition reactions of ·OH or $SO_4^{\bullet-}$, k_{abs} represents the rate constants for abstraction reactions of ·OH or $SO_4^{\bullet-}$, and Γ represents the branching ratio. The formula for calculating Γ is given by $\Gamma = k_i/k_{total}$, where k_{total} is the sum of the rate constants for addition and abstraction reactions of ·OH and $SO_4^{\bullet-}$ with CPY.

Table 1. The total and separated rate constant (k) and branch ratio (Γ) for in the reaction of CPY with ·OH and $SO_4^{\bullet-}$ at 298 K in water system.

Reaction	k_{298K} ($M^{-1}\cdot s^{-1}$)	Γ(%)	Reaction	k_{298K} ($M^{-1}\cdot s^{-1}$)	Γ(%)
CPY+·OH→vdW→IM1-1	3.11×10^8	20.12	CPY+$SO_4^{\bullet-}$→IM1-1(SO_4)	3.89×10^1	0
CPY+·OH→IM1-2(OH)	2.03×10^3	0	CPY+$SO_4^{\bullet-}$→IM1-2(SO_4)	9.62×10^2	0
CPY+·OH→IM1-3(OH)	5.93×10^2	0	CPY+$SO_4^{\bullet-}$→IM1-3(SO_4)	1.61×10^{-1}	0
CPY+·OH→IM1-4(OH)	5.71×10^3	0	CPY+$SO_4^{\bullet-}$→IM1-4(SO_4)	3.30	0
CPY+·OH→IM1-5(OH)	8.12×10^3	0	CPY+$SO_4^{\bullet-}$→IM1-5(SO_4)	8.02×10^2	0
CPY+·OH→IM1-6(OH)	2.60×10^3	0	CPY+$SO_4^{\bullet-}$→IM1-6(SO_4)	7.58	0
CPY+·OH→IM1-7(OH)	2.30×10^{-8}	0	CPY+$SO_4^{\bullet-}$→IM1-7(SO_4)	1.03×10^{-7}	0
k_{add}^{OH}	3.11×10^8	20.12	$k_{add}^{SO_4}$	1.81×10^3	0
CPY+·OH→IM1-8+H_2O	1.51×10^8	9.78	CPY+$SO_4^{\bullet-}$→IM1-8+$HSO_4^{\cdot-}$	1.76×10^8	11.36
CPY+·OH→IM1-9+H_2O	7.80×10^7	5.05	CPY+$SO_4^{\bullet-}$→IM1-9+$HSO_4^{\cdot-}$	7.02×10^8	45.43
CPY+·OH→IM1-10+H_2O	1.08×10^7	0.70	CPY+$SO_4^{\bullet-}$→IM1-10+$HSO_4^{\cdot-}$	2.94	0
CPY+·OH→IM1-11+H_2O	3.52×10^5	0.02	CPY+$SO_4^{\bullet-}$→IM1-11+$HSO_4^{\cdot-}$	8.77×10^5	0.06
CPY+·OH→IM1-12+H_2O	4.47×10^6	0.29	CPY+$SO_4^{\bullet-}$→IM1-12+$HSO_4^{\cdot-}$	3.35×10^6	0.22
CPY+·OH→IM1-13+H_2O	6.78×10^7	4.39	CPY+$SO_4^{\bullet-}$→IM1-13+$HSO_4^{\cdot-}$	2.71×10^7	1.75
CPY+·OH→IM1-14+H_2O	3.33×10^6	0.21	CPY+$SO_4^{\bullet-}$→IM1-14+$HSO_4^{\cdot-}$	4.52×10^6	0.29
CPY+·OH→IM1-15+H_2O	3.04×10^6	0.20	CPY+$SO_4^{\bullet-}$→IM1-15+$HSO_4^{\cdot-}$	8.36×10^3	0
CPY+·OH→IM1-16+H_2O	2.96×10^5	0.02	CPY+$SO_4^{\bullet-}$→IM1-16+$HSO_4^{\cdot-}$	2.03×10^3	0
CPY+·OH→IM1-17+H_2O	1.68×10^6	0.11	CPY+$SO_4^{\bullet-}$→IM1-17+$HSO_4^{\cdot-}$	8.14×10^3	0
CPY+·OH→IM1-18+H_2O	2.67×10^{-3}	0	CPY+$SO_4^{\bullet-}$→IM1-18+$HSO_4^{\cdot-}$	1.75×10^{-4}	0
k_{abs}^{OH}	3.21×10^8	20.77	$k_{abs}^{SO_4}$	9.14×10^8	59.11

When the temperature is 298 K, the Γ of different reaction pathways are as follows: the abstraction reaction between $SO_4^{\bullet-}$ and C_9 atom had the highest Γ (45.43%), followed by the addition reaction between P=S bond and ·OH (20.12%); the abstraction reaction between $SO_4^{\bullet-}$ and C_8 atom (11.36%), and the abstraction reactions between ·OH and C_8 atom, and ·OH and C_8 atom (9.78% and 5.05%, respectively). Lastly, there were the abstraction reactions between the ·OH and C_{13} atom, and between the $SO_4^{\bullet-}$ and C_{13} atom, accounting for 4.39% and 1.75%, respectively. The rest of the reaction pathways could be considered negligible. The calculated total rate constants for the reactions of CPY with ·OH and $SO_4^{\bullet-}$ were 6.32×10^8 and 9.14×10^8 $M^{-1}\cdot s^{-1}$ at 298 K, which was consistent with the experimental values of 4.42×10^9 and 4.5×10^9 $M^{-1}\cdot s^{-1}$ [47]. Results indicated that the calculated results and subsequent theoretical analysis were reliable and valuable.

Pathways with high branching ratios are favorable starting channels [31]. Thus, the corresponding intermediates IM1-1(OH), IM1-8, IM1-9, and IM1-13 were selected as the subjects of study to explore the subsequent reactions of CPY.

3.5. Subsequent Reactions

3.5.1. Subsequent Reactions of IM1-1(OH)

Due to the attack of ·OH, the intermediate IM1-1(OH) became highly reactive with unpaired electrons, thus becoming reactive and capable of generating stable products through its own bond-breaking reactions and H atom abstraction from water (H_2O). The subsequent reactions were illustrated in Figure 6, which involved three pathways. The first pathway involved the cleavage of the P_1–O_{21} bond, resulting in the formation of products P1 (3,5,6-trichloro-2-pyridynol) and the IM2 radical. The IM2 radical further abstracted an H atom from H_2O to produce the stable product P2 (O,O-diethyl phosphorothioate). The

second pathway involved the cleavage of either the P_1–O_{23} or P_1–O_{26} bond. Since these two bond cleavage modes were symmetrical, only the cleavage of the P_1–O_{23} bond was described here. The process led to the formation of P3 and the IM3 radical, which stabilized into product P4 (ethanol) through H atom abstraction reactions. The third pathway involved a bimolecular reaction, where the S atom with unpaired electrons abstracted an H atom from H_2O, followed by the elimination of H_2S to produce P5 (chlorpyrifos oxon). All products except P4 have been detected by HPLC-TOF-MS/MS in the combination system of microwave and persulfate [27]. By comparing the energy barriers of these three pathways, the cleavage of the P_1=O_{21} bond was the most favorable, making it the optimal pathway, which was consistent with the experimental detection of a significant amount of P1 [26,27].

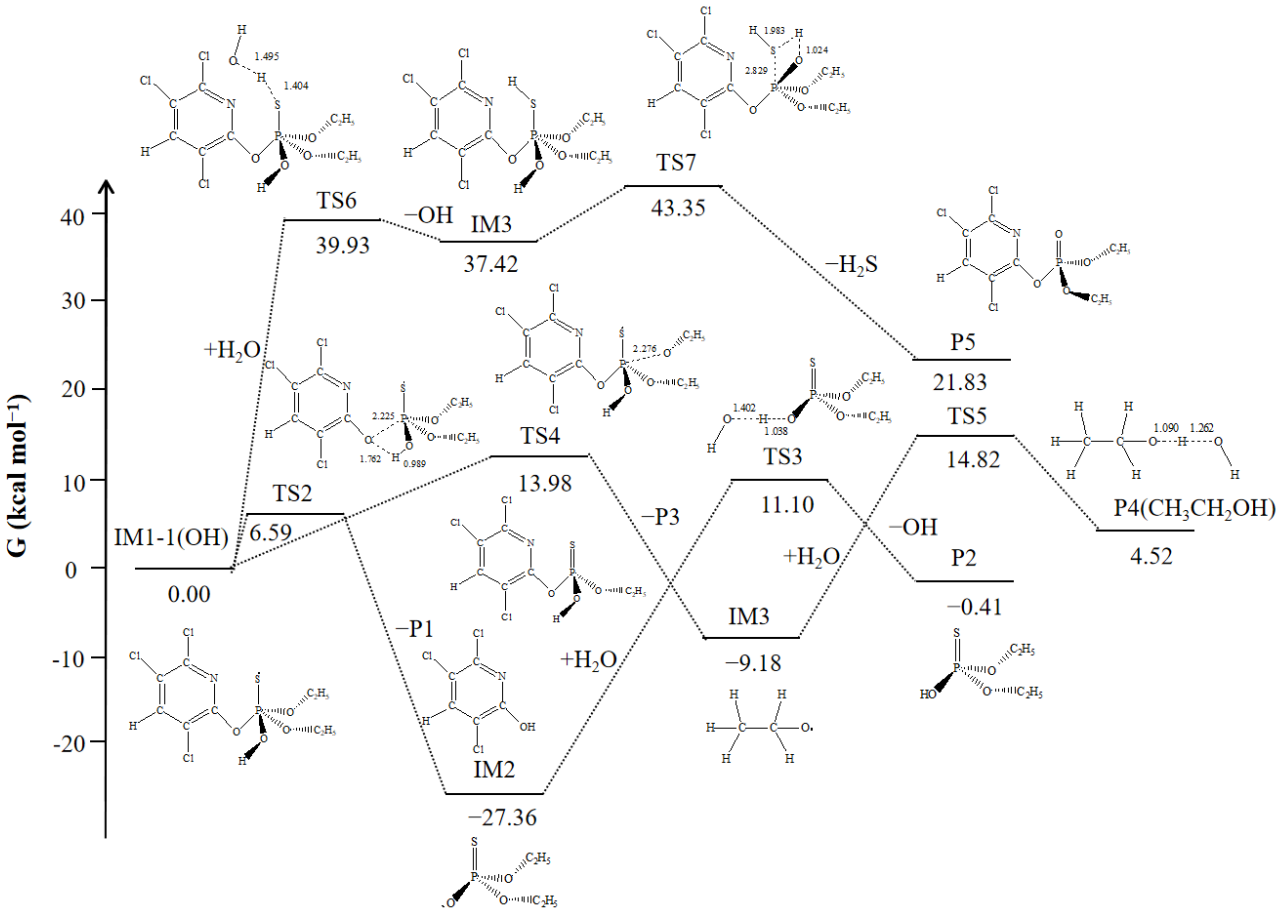

Figure 6. The reaction path profiles of the subsequent reactions of IM-1(OH).

3.5.2. Subsequent Reactions of IM1-8, IM1-9, and IM1-13

The reactions of M1-8, IM1-9, and IM1-13 were very similar, as they all involve barrierless addition with large amount of ·OH present in the solution. As shown in Figure 7, the ΔrG of this process was highly negative, making it easily spontaneous. Subsequently, P7, P8, and P6 (acetaldehyde) are obtained through dealkylation reactions. The $\Delta G^{\neq}$ for these processes range from 16.61 to 18.90 kcal·mol^{-1}, indicating that these reactions are possibly occurred, especially under high-temperature conditions. Corresponding products were also detected in related experimental studies [27].

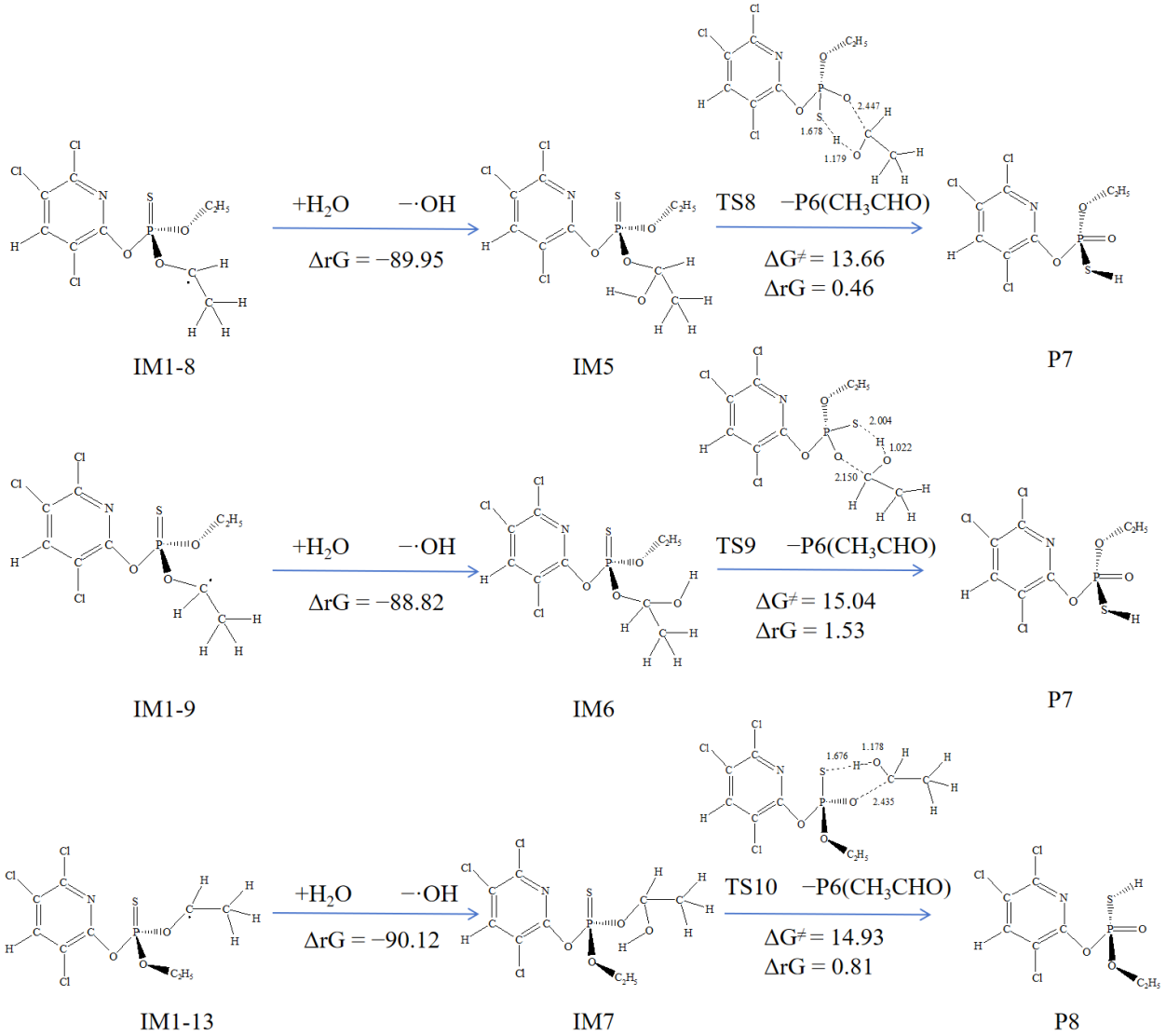

Figure 7. Subsequent reactions of IM1-8, IM1-9, and IM1-13 with the Gibbs free energy barrier $\Delta G^{\neq}$ (kcal·mol^{-1}) and the Gibbs free energy change ΔrG (kcal·mol^{-1}).

In conclusion, in the persulfate-based AOP system, both ·OH and $SO_4^{\bullet-}$ played important roles in the degradation of CPY. The main initiating reactions involved the addition of ·OH to the P=S bond and the H atoms abstraction reactions with the C atoms connected to the P atom. The addition products undergo P_1–O_{21} bond cleavage between the pyridine ring and the P atom, leading to the formation of P1. The abstraction products mainly underwent dealkylation reactions to complete the degradation processes.

3.6. Toxicity Assessment

In this study, the computational toxicity software ECOSAR V2.2 and TEST V5.1.1 were used to assess the eco-toxicity of CPY and its degradation products. Although conducting toxicity experiments is irreplaceable, computational toxicology can conveniently provide a large number of toxicity characteristic values at the screening level. It is widely used in ecological toxicity assessment due to its convenience, speed, cost-effectiveness, and independence from specific experimental animals. Liu et al. used the ECOSAR model to predict the acute and chronic toxicity changes of CPY and its degradation products with ferrate [48]. The results showed that most of the products generated in the later stage of the reaction were classified as non-toxic to all tested organisms. And the dechlorination, ·OH substitution, C–O bond cleavage, and P=S bond oxidation are highly effective in

detoxifying CPY. Shah et al. used the ECOSAR toxicity model on the photocatalytic of CPY to predict the toxicity of its transformation products [25]. The formation of toxic intermediate compounds helps remind researchers to evaluate the toxicity of CPY and the transformation products, and the formation of non-toxic acetate esters as the final product indicates that the treatment technique has significant capabilities for detoxifying CPY.

The ECOSAR ecological toxicity model was used to predict the acute toxicity of CPY and its degradation products to fish, dephnia, and green algae. Table S2 lists the classification criteria for acute and chronic toxicity, while Table S3 lists the acute and chronic toxicity values of CPY and its degradation products. As can be seen, the calculated LC_{50} value of CPY to fish and daphnia are 38 and 0.19 $\mu g \cdot L^{-1}$, respectively, which are in good agreement with the experimental measured results of 25.78 $\mu g \cdot L^{-1}$ for mozambique tilapia and 0.235 to 0.512 $\mu g \cdot L^{-1}$ for daphnia [49,50]. The calculated EC_{50} value of CPY to green algae is 176 $\mu g \cdot L^{-1}$, which is slightly lower than the 769 $\mu g \cdot L^{-1}$ value measured in the experiment [51]. This also demonstrates the accuracy of the computational toxicity prediction method.

Based on the toxicity classification of the Globally Harmonized System (GHS), CPY is defined to be highly toxic compounds [52]. As shown in Figure 8, the toxicity evolution diagram was plotted based on the toxicity classification of the GHS. The acute and chronic toxicity changes indicated that the acute and chronic toxicity of the main degradation products to fish, dephnia, and green algae were lower than that of the parent CPY. However, P1, P2, and P3 still exhibited toxic or highly toxic levels. Therefore, a careful assessment of the potential environmental risks posed by the degradation products is still needed.

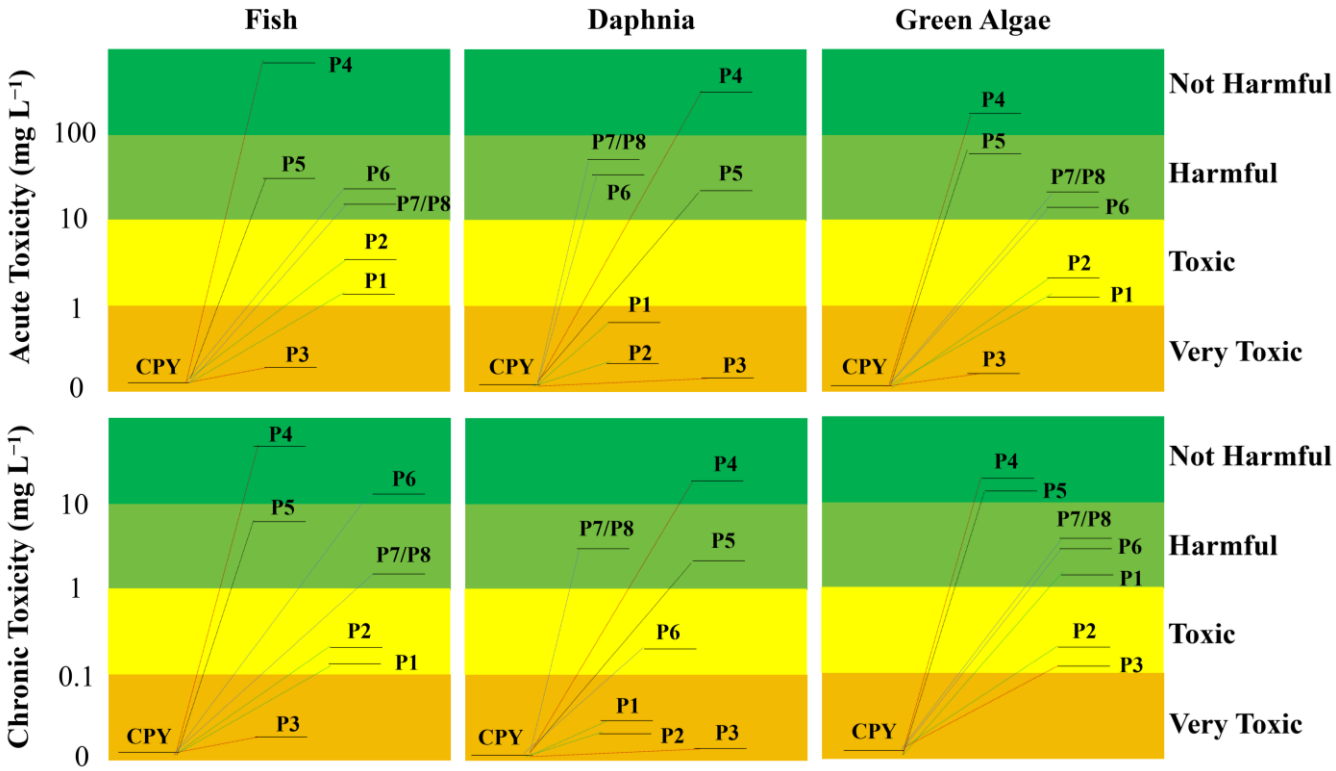

Figure 8. Acute and chronic toxicity of CPY and its transformation products to aquatic organisms.

The TEST software was used to predict the developmental toxicity and mutagenicity of CPY and its products. Table S4 shows that CPY and its products were non-mutagenic. Developmental toxicity could disrupt the homeostasis, normal growth, differentiation, and development of organisms, suggesting that P3, P5, P7, and P8 may have adverse effects on biological development. However, eco-toxicity and health effects were not only dependent on exposure levels but also on bioaccumulation. The bioaccumulation factors

of CPY and its products were much lower than 5000, indicating low bioaccumulation [53]. Low bioaccumulation would not further affect the eco-toxicity and health effects of the compounds. This also suggests that the persulfate-based AOP system could be an effective method to eliminate chlorpyrifos contamination in water environment.

4. Conclusions

In this study, the mechanism of CPY degradation in water environment using persulfate–based AOPs was investigated using the DFT method. The ecological toxicity of CPY and its products was also evaluated. Results indicated that the ·OH and $SO_4^{\bullet-}$ generated from persulfate activation could undergo addition and abstraction reactions with CPY. Thermodynamic and kinetic research indicated that the addition of ·OH to the P=S bond and the abstraction of H atom from the C connected to P atom by both types of active radicals were the main initiating reactions. The reaction rate constants of CPY with ·OH and $SO_4^{\bullet-}$ were 6.32×10^8 and 9.14×10^8 $M^{-1} \cdot s^{-1}$ at room temperature, respectively, which were strongly consistent with experimental data. The addition products underwent the cleavage reaction of the P–O bond between the pyridine ring and the P atom, leading to the formation of the main product of P1. The abstraction products mainly underwent dealkylation reactions to complete the degradation. The acute and chronic toxicities of the main eight degradation products to fish, dephnia, and green algae were found to be lower than those of the parent CPY. However, products of P1, P2, and P3 still exhibited toxic or highly toxic levels, which may pose risks to human health. However, due to their low bioaccumulation, their ecological toxicity and health effects may be limited. Overall, these findings provide theoretical support for the application of persulfate-based AOP system for the removal of eliminating chlorpyrifos contamination in water environment.

Supplementary Materials: The following supporting information can be downloaded at: https://www.mdpi.com/article/10.3390/toxics12030207/s1, Figure S1: The optimized chemical conformations of TS for CPY with ·OH; Figure S2: The optimized chemical conformations of TS for CPY with $SO_4^{\bullet-}$; Table S1: The bond lengths of the calculated values and the experimental values of CPY; Table S2: The grading standards of the acute and chronic toxicity. The unit is $mg \cdot L^{-1}$.; Table S3: The toxicity value of the main transformation intermediates and products in the degradation of CPY. The unit is $mg \cdot L^{-1}$.; Table S4: Estimated health effects of CPY and its transformation intermediates and products during the degradation process.

Author Contributions: Conceptualization, Y.X., C.Z., S.W. and H.T.; methodology, Y.X.; software, Y.X. and C.Z.; validation, Y.X., C.Z. and H.T.; formal analysis, Y.X.; investigation, H.Z. and G.C.; resources, X.S., S.W. and H.T.; data curation, Y.X., H.Z. and G.C.; writing—original draft preparation, Y.X.; writing—review and editing, X.S., S.W. and H.T.; visualization, Y.X. and C.Z.; supervision, S.W. and H.T.; project administration, C.Z., S.W. and H.T.; funding acquisition, Y.X., C.Z., S.W. and H.T. All authors have read and agreed to the published version of the manuscript.

Funding: This research was funded by National Natural Science Foundation of China (grant number 52200198, U20A20146), the Natural Science Foundation of Shandong Province (grant number ZR2021QB186), the Science and Technology Development Program of Weifang City (grant number 2022GX036, 2023GX054), the Science and Technology Development Program of Shouguang City (grant number 2022JH08) and the Fundamental Research Funds of Weifang University of Science and Technology (grant number KJRC2022013).

Institutional Review Board Statement: Not applicable.

Informed Consent Statement: Not applicable.

Data Availability Statement: Data are contained within the article.

Conflicts of Interest: The authors declare no conflicts of interest.

References

1. Wołejko, E.; Łozowicka, B.; Jabłońska-Trypuć, A.; Pietruszyńska, M.; Wydro, U. Chlorpyrifos occurrence and toxicological risk assessment: A review. *Int. J. Environ. Res. Public. Health* **2022**, *19*, 12209. [CrossRef] [PubMed]
2. Bose, S.; Kumar, P.S.; Dai-Viet, N.V. A review on the microbial degradation of chlorpyrifos and its metabolite TCP. *Chemosphere* **2021**, *283*, 131447. [CrossRef] [PubMed]
3. Sud, D.; Kumar, J.; Kaur, P.; Bansal, P. Toxicity, natural and induced degradation of chlorpyrifos. *J. Chil. Chem. Soc.* **2020**, *65*, 4807–4816. [CrossRef]
4. Huang, X.; Cui, H.; Duan, W. Ecotoxicity of chlorpyrifos to aquatic organisms: A review. *Ecotox. Environ. Safe.* **2020**, *200*, 110731. [CrossRef] [PubMed]
5. Gül, A. Investigation of acute toxicity of chlorpyrifos-methyl on Nile tilapia (*Oreochromis niloticus* L.) larvae. *Chemosphere* **2005**, *59*, 163–166. [CrossRef] [PubMed]
6. Foong, S.Y.; Ma, N.L.; Lam, S.S.; Peng, W.; Low, F.; Lee, B.H.K.; Alstrup, A.K.O.; Sonne, C. A recent global review of hazardous chlorpyrifos pesticide in fruit and vegetables: Prevalence, remediation and actions needed. *J. Hazard. Mater.* **2020**, *400*, 123006. [CrossRef] [PubMed]
7. Mackay, D.; Giesy, J.P.; Solomon, K.R. Fate in the Environment and Long-Range Atmospheric Transport of the Organophosphorus Insecticide, Chlorpyrifos and Its Oxon. *Rev. Environ. Contam. Toxicol.* **2014**, *231*, 35–76.
8. Sumon, K.A.; Rashid, H.; Peeters, E.T.; Bosma, R.H.; Van den Brink, P.J. Environmental monitoring and risk assessment of organophosphate pesticides in aquatic ecosystems of north-west Bangladesh. *Chemosphere* **2018**, *206*, 92–100. [CrossRef]
9. Stalin, A.; Suganthi, P.; Mathivani, S.; Paray, B.A.; Al-Sadoon, M.K.; Gokula, V.; Musthafa, M.S. Impact of chlorpyrifos on behavior and histopathological indices in different tissues of freshwater fish *Channa punctatus* (Bloch). *Environ. Sci. Pollut. Control Ser.* **2019**, *26*, 17623–17631. [CrossRef]
10. Bootharaju, M.S.; Pradeep, T. Understanding the Degradation Pathway of the Pesticide, Chlorpyrifos by Noble Metal Nanoparticles. *Langmuir* **2012**, *28*, 2671–2679. [CrossRef]
11. Perry, J.; Cotton, J.; Rahman, M.A.; Brumby, S. Organophosphate Exposure and the Chronic Effects on Farmers: A Narrative Review. *Rural. Remote Health* **2020**, *20*, 4508. [CrossRef] [PubMed]
12. Hazarika, J.; Ganguly, M.; Borgohain, G.; Sarma, S.; Bhuyan, P.; Mahanta, R. Disruption of androgen receptor signaling by chlorpyrifos (CPF) and its environmental degradation products: A structural insight. *J. Biomol. Struct. Dyn.* **2022**, *40*, 6027–6038. [CrossRef] [PubMed]
13. Jiang, F.; Wu, W.Q.; Zhu, Z.W.; Zhu, S.S.; Wang, H.X.; Zhang, L.; Fan, Z.Y.; Chen, Y.Q. Structure identification and toxicity evaluation of one newly-discovered dechlorinated photoproducts of chlorpyrifos. *Chemosphere* **2022**, *301*, 134822. [CrossRef] [PubMed]
14. Aswathi, A.; Pandey, A.; Sukumaran, R.K. Rapid degradation of the organophosphate pesticide–Chlorpyrifos by a novel strain of Pseudomonas nitroreducens AR-3. *Bioresour. Technol.* **2019**, *292*, 122025. [CrossRef] [PubMed]
15. Xu, Z.; Chen, X.Y.; Jin, X.; Hu, S.H.; Lan, Y.; Xi, W.H.; Han, W.; Cheng, C. Study on the effective removal of chlorpyrifos from water by dielectric barrier discharge (DBD) plasma: The influence of reactive species and different water components. *Chem. Eng. J.* **2023**, *473*, 144755. [CrossRef]
16. Esfandian, H.; Cherati, M.R.; Khatirian, M. Electrochemical behavior and photocatalytic performance of chlorpyrifos pesticide decontamination using Ni-doped ZnO-TiO_2 nanocomposite. *Inorg. Chem. Commun.* **2024**, *159*, 111750. [CrossRef]
17. Jacob, M.M.; Ponnuchamy, M.; Kapoor, A.; Sivaraman, P. Bagasse based biochar for the adsorptive removal of chlorpyrifos from contaminated water. *J. Environ. Chem. Engin.* **2020**, *8*, 103904. [CrossRef]
18. Dolatabadi, M.; Naidu, H.; Ahmadzadeh, S. Adsorption characteristics in the removal of chlorpyrifos from groundwater using magnetic graphene oxide and carboxy methyl cellulose composite. *Sep. Purif. Technol.* **2022**, *300*, 121919. [CrossRef]
19. Hadibarata, T.; Kristanti, R.A.; Bilal, M.; Yilmaz, M.; Sathishkumar, P. Biodegradation mechanism of chlorpyrifos by halophilic bacterium *Hortaea* sp. B15. *Chemosphere* **2023**, *312*, 137260. [CrossRef] [PubMed]
20. Liu, C.; Zhao, C.Y.; Wang, L.J.; Du, X.M.; Zhu, L.S.; Wang, J.; Kim, Y.M.; Wang, J.H. Biodegradation mechanism of chlorpyrifos by *Bacillus* sp. H27: Degradation enzymes, products, pathways and whole genome sequencing analysis. *Environ. Res.* **2023**, *239*, 117315. [CrossRef] [PubMed]
21. Teymourinia, H.; Alshamsi, H.A.; Al-Nayili, A.; Gholami, M. Photocatalytic degradation of chlorpyrifos using Ag nanoparticles-doped g-C_3N_5 decorated with dendritic CdS. *Chemosphere* **2023**, *344*, 140325. [CrossRef]
22. Zhang, Y.; Zhou, B.; Chen, H.; Yuan, R. Heterogeneous photocatalytic oxidation for the removal of organophosphorus pollutants from aqueous solutions: A review. *Sci. Total Environ.* **2023**, *856*, 159048. [CrossRef]
23. Sheikhi, S.; Dehghanzadeh, R.; Aslani, H. Advanced oxidation processes for chlorpyrifos removal from aqueous solution: A systematic review. *J. Environ. Health Sci.* **2021**, *19*, 1249–1262. [CrossRef] [PubMed]
24. Gandhi, K.; Lari, S.; Tripathi, D.; Kanade, G. Advanced oxidation processes for the treatment of chlorpyrifos, dimethoate and phorate inaqueous solution. *J. Water Reuse Desal.* **2016**, *6*, 195–203. [CrossRef]

25. Shah, N.S.; Iqbal, J.; Sayed, M.; Ghfar, A.A.; Khan, J.A.; Khan, Z.U.H.; Murtaza, B.; Boczkaj, G.; Jamil, F. Enhanced solar light photocatalytic performance of Fe-ZnO in the presence of H_2O_2, $S_2O_8^{2-}$, and HSO_5^- for degradation of chlorpyrifos from agricultural wastes: Toxicities investigation. *Chemosphere* **2022**, *287*, 132331. [CrossRef] [PubMed]
26. Xie, H.L.; Xu, W.G. Enhanced activation of persulfate by meso-$CoFe_2O_4/SiO_2$ with ultrasonic treatment for degradation of chlorpyrifos. *ACS Omega* **2019**, *4*, 17177–17185. [CrossRef] [PubMed]
27. Shang, X.; Liu, X.T.; Ren, W.B.; Huang, J.; Zhou, Z.; Lin, C.; He, M.C.; Ouyang, W. Comparison of peroxodisulfate and peroxymonosulfate activated by microwave for degradation of chlorpyrifos in soil: Effects of microwaves, reaction mechanisms and degradation products. *Sep. Purif. Technol.* **2023**, *306*, 122682. [CrossRef]
28. Zhang, C.X.; Xu, Y.X.; Liu, W.Y.; Zhou, H.Y.; Zhang, N.N.; Fang, Z.H.; Gao, J.P.; Sun, X.A.; Feng, D.; Sun, X.M. New insights into the degradation mechanism and risk assessment of HFPO-DA by advanced oxidation processes based on activated persulfate in aqueous solutions. *Ecotoxicol. Environ. Saf.* **2023**, *263*, 115298. [CrossRef]
29. Quintano, M.M.; Rodrigues, G.L.; Chagas, M.A.; Rocha, W.R. Revisiting the tropospheric OH-initiated unimolecular decomposition of chlorpyrifos and chlorpyrifos-methyl: A theoretical perspective. *J. Phys. Chem. A* **2020**, *124*, 4280–4289. [CrossRef]
30. Zhou, Q.; Sun, X.Y.; Gao, R.; Zhang, Q.Z.; Wang, W.X. Mechanism study on OH-initiated atmospheric degradation of the organophosphorus pesticide chlorpyrifos. *J. Mol. Struc-Theochem.* **2010**, *952*, 8–15. [CrossRef]
31. Zhao, H.; Wang, S.J.; Zhang, Y.J.; Lu, C.G.; Tang, Y.Z. Degradation of mevinphos and monocrotophos by OH radicals in the environment: A computational investigation on mechanism, kinetic, and ecotoxicity. *J. Hazard. Mater.* **2023**, *445*, 130478. [CrossRef]
32. Cao, X.S.; Zhu, F.P.; Zhang, C.X.; Sun, X.M. Degradation of UV-P mediated by hydroxyl radical, sulfate radical and singlet oxygen in aquatic solution: DFT and experimental studies. *Environ. Pollut.* **2022**, *315*, 120416. [CrossRef]
33. Xu, Y.X.; Zhang, C.X.; Wang, Z.; Chen, B.; Sun, X.M.; Wang, S.G.; Tian, H.F. Novel insights into the dehalogenation mechanism and ecotoxicity assessment of 6:2 Cl-PFESA from density functional theory calculations. *Emerg. Contam.* **2024**, *10*, 100301. [CrossRef]
34. Frisch, M.J.; Trucks, G.W.; Schlegel, H.B.; Scuseria, G.E.; Robb, M.A.; Cheeseman, J.R.; Scalmani, G.; Barone, V.; Petersson, G.A.; Nakatsuji, H.; et al. *Gaussian 16 Rev. A.03*; Gaussian: Wallingford, CT, USA, 2016.
35. Zhao, Y.; Truhlar, D.G. The M06 suite of density functionals for main group thermochemistry, thermochemical kinetics, noncovalent interactions, excited states, and transition elements: Two new functionals and systematic testing of four M06- class functionals and 12 other functionals. *Theor. Chem. Acc.* **2008**, *120*, 215–241.
36. Maeda, S.; Harabuchi, Y.; Ono, Y.; Taketsugu, T.; Morokuma, K. Intrinsic reaction coordinate: Calculation, bifurcation, and automated search. *Int. J. Quantum Chem.* **2015**, *115*, 258–269. [CrossRef]
37. Marenich, A.V.; Cramer, C.J.; Truhlar, D.G. Universal solvation model based on solute electron density and on a continuum model of the solvent defined by the bulk dielectric constant and atomic surface tensions. *J. Phys. Chem. B.* **2009**, *113*, 6378–6396. [CrossRef]
38. Xu, M.M.; Yan, S.D.; Sun, S.M.; Ni, Z.R.; Wu, W.Z.; Sun, J.Y. N, N-diethyl-m-toluamide (DEET) degradation by •OH and $SO_4^{\bullet-}$-assisted AOPs in wastewater treatment: Theoretical studies into mechanisms, kinetics and toxicity. *J. Environ. Chem. Eng.* **2022**, *10*, 108435. [CrossRef]
39. Sun, J.; Chu, R.; Khan, Z.U.H. A Theoretical study on the degradation mechanism, kinetics, and ecotoxicity of metronidazole (MNZ) in •OH- and $SO_4^{\bullet-}$-assisted advanced oxidation processes. *Toxics* **2023**, *11*, 796. [CrossRef]
40. Canneaux, S.; Bohr, F.; Henon, E. KiSThelP: A program to predict thermodynamic properties and rate constants from quantum chemistry results. *J. Comput. Chem.* **2014**, *35*, 82–93. [CrossRef] [PubMed]
41. Laidler, K.J. *Theories of Chemical Reaction Rates*; McGraw-Hill Book Company: New York, NY, USA, 1969.
42. Shiroudi, A.; Deleuze, M.S. Theoretical study of the oxidation mechanisms of naphthalene initiated by hydroxyl radicals: The H abstraction pathway. *J. Phys. Chem. A* **2014**, *118*, 4593–4610. [CrossRef] [PubMed]
43. U.S. EPA. *Ecological Structure—Activity Relationships Program (ECOSAR) Operation Manual, v2.2*; U.S. EPA: Washington, DC, USA, 2022.
44. U.S. EPA. *Toxicity Estimation Software Tool, version 5.1.1*; U.S. EPA: Washington, DC, USA, 2022.
45. Baughman, R.G.; Jorgenson, S.K.; Jacobson, R.A. The crystal and molecular structure of organophosphorus insecticides. 10. Chlorpyrifos. *J. Agric. Food Chem.* **1978**, *26*, 576–590. [CrossRef]
46. Ding, X.Y.; Song, X.; Chen, X.; Ding, D.; Xu, C.; Chen, H. Degradation and mechanism of hexafluoropropylene oxide dimer acid by thermally activated persulfate in aqueous solutions. *Chemosphere* **2022**, *286*, 131720. [CrossRef]
47. Shah, N.S.; Khan, J.A.; Sayed, M.; Khan, Z.U.H.; Iqbal, J.; Imran, M.; Murtaza, B.; Zakir, A.; Polychronopoulou, K. Nano zerovalent zinc catalyzed peroxymonosulfate based advanced oxidation technologies for treatment of chlorpyrifos in aqueous solution: A semi-pilot scale study. *J. Clean. Prod.* **2020**, *246*, 119032. [CrossRef]
48. Liu, H.X.; Chen, J.; Wu, N.N.; Xu, X.X.; Qi, Y.M.; Jiang, L.J.; Wang, X.H.; Wang, Z.Y. Oxidative degradation of chlorpyrifos using ferrate (VI): Kinetics and reaction mechanism. *Ecotox. Environ. Safe.* **2019**, *170*, 259–266. [CrossRef]
49. Rao, J.V. Brain acetylcholinesterase activity as a potential biomarker for the rapid assessment of chlorpyrifos toxicity in a euryhaline fish, *Oreochromis mossambicus*. *Environ. Bioindic.* **2008**, *3*, 11–22.
50. Zalizniak, L.; Nugegoda, D. Effect of sublethal concentrations of chlorpyrifos on three successive generations of Daphnia carinata. *Ecotox. Environ. Saf.* **2006**, *64*, 207–214. [CrossRef] [PubMed]

51. DeLorenzo, M.E.; Serrano, L. Individual and mixture toxicity of three pesticides; atrazine, chlorpyrifos, and chlorothalonil to the marine phytoplankton species *Dunaliella* tertiolecta. *J. Environ. Sci. Health B* **2003**, *38*, 529–538. [CrossRef] [PubMed]
52. United Nations Economic Commission for Europe (UNECE). *Globally Harmonized System of Classification and Labelling of Chemicals (GHS)*; UN: New York, NY, USA; Geneva, Switzerland, 2011.
53. He, M.J.; Luo, X.J.; Chen, M.Y.; Sun, Y.X.; Chen, S.J.; Mai, B.X. Bioaccumulation of polybrominated diphenyl ethers and decabromodiphenyl ethane in fish from a river system in a highly industrialized area, South China. *Sci. Total Environ.* **2012**, *419*, 109–115. [CrossRef] [PubMed]